International Journal of Solids and Structures 51 (2014) 1859–1871

Contents lists available at ScienceDirect

International Journal of Solids and Structures

journal homepage: www.elsevier.com/locate/ijsolstr

A continuum model for intermittent deformation of single crystal micropillars

Xu Zhang, Fulin Shang *

State Key Laboratory for Strength and Vibration of Mechanical Structures, School of Aerospace, Xi'an Jiaotong University, Xi'an 710049, PR China

ARTICLE INFO

Article history:
Received 13 September 2013
Received in revised form 24 October 2013
Available online 11 November 2013

Keywords:
Single crystal metal
Micropillar
Plasticity
Strain burst
Continuum model

ABSTRACT

Strain bursts are often observed during compression tests of single crystal micropillars. In this work, we formulate a new continuum model that accounts for the strain bursts within the framework of crystal plasticity. The strain bursts are separated from the loading stage (nearly elastic loading) by introducing a dimensionless constant in the continuum model, and are detected by load serrations. The boundary conditions in the context of micropillar compression are studied and they are shown to be changing and unpredictable as plastic deformation proceeds. To evaluate the validity of our model, finite element simulations of the uniaxial compression tests on nickel micropillars are performed. Our simulations produce clearly visible strain bursts during the plastic flow and the produced intermittent flows are comparable with the experimental observations. For the bulk crystal, a series of strain bursts is identified in the course of plastic flow, despite an apparently smooth stress–strain response. We also show that the intermittent flow is intensified in the micrometer-scale due to both increasing numbers of the successive strain bursts and increasing amplitude of the strain burst, when the specimen size decreases. Finally, we show that the occurrences of the strain bursts are always associated with negative values of the second-order work.

1. Introduction

The plastic deformation behavior of bulk single crystals have been successfully described by classical continuum mechanics of plasticity, and have been demonstrated to be associated with a steady rate of work hardening. Many recent compression experiments of single crystal micropillars show that their plastic deformations are characterized by large intrinsic fluctuations (strain bursts) and the yield strength is size-dependent (Greer and Nix, 2006; Uchic et al., 2004). These fluctuations that are usually caused by the collective motion of interacting dislocation, lead to a strongly heterogeneous and intermittent nature of plastic flow on microscopic and mesoscopic scales, whereas in bulk crystals plasticity appears as a smooth and homogeneous process. The strain burst phenomenon is suggested to be universal in plasticity and independent of pillar dimensions (Csikor et al., 2007).

To better understand the crystal plasticity at microscopic level, there have been many studies using three-dimensional (3-D) dislocation dynamics (DD) simulations (3D-DDS) (Csikor et al., 2007; Tang et al., 2008) and multiscale modeling (Akarapu et al., 2010). These simulations show that the strain bursts arise from the continuous operation of one or at most a few dislocation sources (Akarapu et al., 2010; Tang et al., 2008) or the destruction of jammed dislocation configurations (Csikor et al., 2007). In particular, some DD techniques could well reproduce the essential aspects of experimental observations on burst activities (Csikor et al., 2007). In addition, numerical algorithms have also been developed to study such activities (Greer and Nix, 2006; Zaiser and Aifantis, 2006; Zhang and Aifantis, 2011). For example, Greer and Nix (2006) developed a numerical iterative algorithm based on the phenomenological model of dislocation starvation, and captured one single strain burst followed by elastic loading. Zhang and Aifantis (2011) have proposed a strain gradient model from the point of view that plastic deformation occurs through slip zones in the gauge region. These slip zones are divided into elastic and plastic zones and a strain burst occurs when two adjacent zones deform plastically. In such models, the predicted results are in good agreement with the experimental stress–strain curves. Besides such simulation efforts, some statistic models have been proposed to study the characteristics of intermittent flow behavior of small microcrystal (Ng and Ngan, 2008; Ngan and Ng, 2010). Although prior knowledge of survival probability of occurrence for burst events and stress-dependent distributions of burst sizes are required as two inputs to incorporate into these models, the calcu-

* Corresponding author. Tel./fax: +86 29 82665490.
E-mail address: shangfl@mail.xjtu.edu.cn (F. Shang).

http://dx.doi.org/10.1016/j.ijsolstr.2013.11.002
0020-7683/

lated results successfully predict other aspects of microcrystal deformation in terms of the intermittent stress–strain response, stress-dependent burst size and power-law behavior of burst events. These results are consistent with the experimental observations. Furthermore, such inputs obtained from one loading condition can also be applied to other loading situations such as creep deformation (Ng and Ngan, 2008; Ngan and Ng, 2010). In addition, statistical theory analysis suggests that the mechanism of the burst activities is related to the continuous activation of a few dislocation sources (Ngan and Ng, 2010).

Alternatively, finite element methods (FEM) using continuum models of plasticity such as crystal plasticity or gradient plasticity are comparatively less used to study intermittent plasticity. Although it has been suggested that strain bursts are associated with deformation patterns in the form of slip lines and slip bands (Csikor et al., 2007; Schwerdtfeger et al., 2010), they are not necessarily or may not always give rise to macroscopic deformation instabilities. As observed in submicron diameter compression tests (Greer and Nix, 2006; Uchic et al., 2004), plastic deformation occurs in a non-localized manner until sufficiently larger strain and the experimental stress–strain curves are relatively smooth. As a result, employment of the continuum crystal plasticity theory to obtain a better understanding of micropillar plasticity may be warranted (Hurtado and Ortiz, 2012; Kuroda, 2013). Additionally, the corresponding boundary-value problems may also be well-posed and thus contribute to the uniqueness and convergence of the solutions in the finite element calculations. In fact, finite element simulations using crystal plasticity theory have been conducted to study the influence of extrinsic effects such as friction and sample geometry, which are involved in micro-compression tests (Choi et al., 2007; Raabe et al., 2007; Shade et al., 2009). Furthermore, several finite element implementations of phenomenological models have recently been employed to investigate the effect of physics on micropillar deformation, such as dislocation nucleation and starvation (Jérusalem et al., 2012), or the self-energy of the dislocations and the energy of dislocation steps at the boundary of the solid (Hurtado and Ortiz, 2012), as well as higher-order gradients arising from geometrically necessary dislocation densities (Kuroda, 2013).

All of the above phenomenological FEM analyses have mainly focused on size effects of the yield strength. However, intermittent deformations have not been reflected in these simulations. This is partly because, conventional continuum theories of plasticity do not reflect the characteristics of strain burst and contain no criteria to judge the stain burst, and hence fail in predicting its occurrence. Besides, there is one problem lying in variability and unpredictability of the microscopic boundary conditions (MBCs) as the plastic flow proceeds. For example, many micro-compression tests are driven by hybrid loading mode (HLM) (El-Awady et al., 2013; Papanikolaou et al., 2012; Uchic et al., 2004), in which a mixture of constant displacement rate and creep-like loading conditions are employed. This method produces a staircase-like stress–strain curve, which is characterized by a nearly constant stress within the strain burst period and a purely elastic strain during the loading stage. Normally, the strain bursts are separated by increments of nearly elastic loading stage during the plastic flow (El-Awady et al., 2013). This phenomenon leads to a change of MBCs during plastic deformations, since the loading system responds differently to the burst slip and the loading stage under the condition of HLM (Uchic and Dimiduk, 2005). This means that the MBCs are time-dependent in the plastic deformation process.

In this paper, we focus on the intermittent flow of micropillars and aim to develop a new continuum model to describe such phenomenon. For this purpose, our continuum model takes into account the following key elements: (i) Separation of the burst slip from loading stage: This is motivated by the difference in features between the burst slip and the loading stage. The burst slip occurs at a high strain rate and is associated with stress relaxation. The loading stage, however, is characterized by a slow strain rate and is associated with continuous increase in load; (ii) A criterion to judge the appearance of the stain burst: This is motivated by the loading system, since it responds differently to the burst slip and loading stage (Uchic and Dimiduk, 2005), resulting in different MBCs for the two cases. Thus, the continuum model should contain a criterion to demarcate the burst slip from the loading stage, similar to the yield stress that demarcates the elastic loading from the plastic flow; (iii) Solution of the problems with time-dependent MBCs: This is motivated by the unpredictability of the MBCs, since the occurrence of the burst slips and their amplitudes are unpredictable. In other words, the MBCs are not predetermined.

This paper is organized as follows: In Section 2, the microscopic boundary conditions in the context of intermittent flow are discussed. In Section 3, the continuum model is proposed in the framework of crystal plasticity (Peirce et al., 1983). To verify our model, Section 4 presents the finite element algorithm of implementing our proposed continuum model, and comparisons are made between our present model and the crystal-plasticity finite element method (CPFEM). In Section 5, the finite element simulations of the uniaxial compression tests on face-centered cubic (FCC) nickel micropillars are described. Finally, the results of Sections 4 and 5 are discussed for further improvements of the proposed model in Sections 6, and the conclusions are presented in Section 7.

2. Problem formulation

The problem considered is graphically represented in Fig. 1(a) and (b). Fig. 1(a) shows the actual displacement vs. time curve obtained from the micro-compression tests on a ~20 μm diameter Ni micropillar under conditions of HLM. Fig. 1(b) shows the schematic plot of the micro-compression test driven by the HLM, which is the simplified and idealized representation of Fig. 1(a). Note that a strain burst is generally characterized by a larger strain increment and a smaller time increment (Dimiduk et al., 2006, 2010), indicating a higher strain rate in a burst slip, compared to that of the loading stage. Thus, the curve portion with positive slope in Fig. 1(b), which has a higher rate than that of constant loading, represents the occurrence of a burst slip. The burst slip is followed by a horizontal line or a line with small positive slope, which indicates a holding stage and it lasts until the actual micropillar displacement reaches the imposed displacement by the nanoindentation system. A loading stage may occur after this, associated with the constant strain-rate loading process. On the basis of these observations, a typical plastic flow expressed in the stress–strain curve normally includes three distinct parts: loading stage ΔE^{l}, burst slip part ΔE^{b} and holding stage ΔE^{h}, where superscripts l, b and h represent the above three processes, respectively (see inset in Fig. 1(b)).

2.1. Loading stage

The loading stage involves the motion of few dislocations, while majority other dislocations are relatively immobile, making little or no contribution to the strain. Thus, many of the nearly elastic zones between strain bursts are frequently observed from the stress–strain curves of micro-compression tests (El-Awady et al., 2013; Papanikolaou et al., 2012; Uchic et al., 2004). Such a stage is induced when the applied load becomes comparable to the internal stress of the micropillar, and the displacement on the top surface of micropillar is kept consistent with the pre-programmed displacement of the indention platen controlled by a feedback control loop (see Fig. 1). As a result, the engineering strain increment ΔE^{l} produced by the imposed displacement Δu^{l}, is only determined by the time increment Δt^{l} due to the applied constant strain rate $\dot{\varepsilon}_0$, and it follows that:

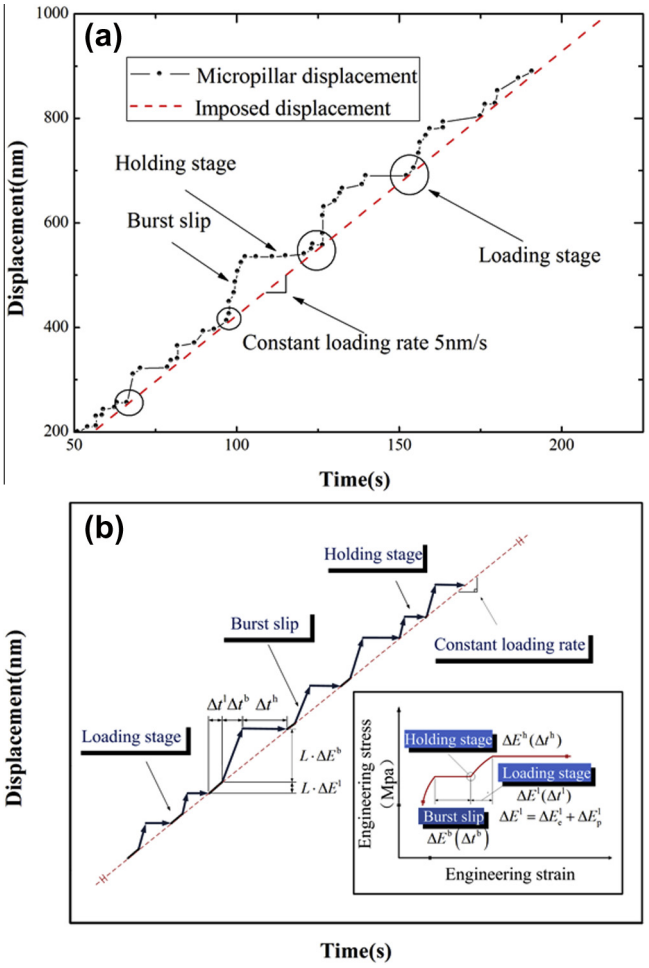

Fig. 1. (a) True experimental and (b) schematic drawing of displacement vs. time curve taken from the micro-compression test of ~20 μm diameter Ni micropillar driven by the HLM. The Red and black line represent the applied loading displacement by the nanoindentation system and the displacements of micropillar on the top surface, respectively. Inset: the schematic drawing of stress–strain curve. (For interpretation of the references to color in this figure legend, the reader is referred to the web version of this article.)

$$\Delta E^{\mathrm{l}}(\Delta t^{\mathrm{l}}) = \dot{\varepsilon}_0 \cdot \Delta t^{\mathrm{l}} \tag{1}$$

where ΔE^{l} consists of two parts: the elastic strain $\Delta E^{\mathrm{l}}_{\mathrm{e}}$ (if unloading, it is recovered) and the plastic strain $\Delta E^{\mathrm{l}}_{\mathrm{p}}$ (see inset in Fig. 1(b)), which arises from the slip of few dislocations inside the micropillar.

2.2. Burst slip

The burst slip arises from the collective, avalanche-like motion of the dislocations, thus resulting in a sudden surge of the displacement increment on the top surface of the specimen. On one hand, the nanoindentation system employs a voice coil as the force actuator and uses the springs to suspend the indentation platen. Such a displacement burst can cause the springs to become suddenly elongated, causing a drop in the load that is applied on the sample. Nevertheless, the springs mounted on the nanoindentation system are often very compliant; thus a very small load drop would take place. Compared to the cumulative load applied on the specimen, such load drop could be reasonably neglected. Thus, within the burst duration Δt^{b}, the engineering stress increment $\Delta\Sigma^{\mathrm{b}}$ produced by such small load drops could be idealized as:

$$\Delta\Sigma^{\mathrm{b}}(\Delta t^{\mathrm{b}}) = 0 \tag{2}$$

On the other hand, a burst slip occurs at a faster rate than $\dot{\varepsilon}_0$. Comparing with the loading stage, the burst slip process is generally characterized by the larger strain increment ΔE^{b} and smaller time increment Δt^{b}. The concrete relationship between ΔE^{b} and slip duration Δt^{b} is unknown. However, the engineering strain increment ΔE^{b} can be written in another form as:

$$\Delta E^{\mathrm{b}}(\Delta t^{\mathrm{b}}) = \delta E \tag{3}$$

Here, δE is the magnitude of the strain burst, and its value follows a statistical distribution having a general form (Csikor et al., 2007):

$$p(\delta E) = C(\delta E)^{-\eta} \exp\left[-(\delta E/\delta E_{\max})^2\right] \tag{4}$$

In Eq. (4), C is the normalization constant and $\delta E_{\max}$ is the cut-off strain of the largest avalanche. The material-independent exponent η is reported to be 1.35 (Zhang et al., 2012). It should be mentioned that Eq. (4) describes the overall behavior of the burst sizes. Specifically, as observed from experiments, the burst size is also of history dependence on the stress (Ng and Ngan, 2008), and the burst size generally increases with the increase of the stress.

2.3. Holding stage

The holding stage follows the burst slip. As mentioned above, the burst slip results in a small load drop in the total applied force, causing its value to be smaller than the internal stress of the specimen. As a result, the top surface of micropillar stops moving until the applied force becomes comparable in magnitude to the internal stress. As such a process proceeds, there are always finite plastic displacements occurring in terms of creep strain induced by cross-slip or other slower relaxation processes (Papanikolaou et al., 2012). However, the strain increments produced by these complexities appear to be negligible since the displacement vs. time curves within the holding sections always exhibit small positive slopes (see Fig. 1(a)). For these two reasons, the engineering strain increment ΔE^{h}, which is produced by the above mentioned finite displacements within each holding section, is not considered (see inset in Fig. 1(b)) and in an ideal case one has:

$$\Delta E^{\mathrm{h}}(\Delta t^{\mathrm{h}}) = 0 \tag{5}$$

Since the above mentioned finite displacements within each holding stage are small, they would cause the springs to be elongated slightly. As a result, the induced load drop is expected to be much smaller due to the compliant nature of the springs. Hence, the engineering stress increment $\Delta\Sigma^{\mathrm{h}}$ within the whole holding stage takes the ideal form as:

$$\Delta\Sigma^{\mathrm{h}}(\Delta t^{\mathrm{h}}) = 0 \tag{6}$$

Thus, Eqs. (1)–(6) describe the representative MBCs of the micropillar plasticity, and it is worth mentioning that they vary as the plastic deformation proceeds. They are also shown to be unpredictable because the occurrence of a burst slip cannot be predicted. Even when a burst slip event occurs, the value of its MBCs is still unpredictable due to the stochastic nature of the burst size, as described in Eq. (4).

3. Continuum crystal plasticity model

Crystal plasticity theory is considered to be a physical theory, in which the collective dislocation movement on slip systems is represented in a continuum sense as plastic shear strain, and it combines continuum theory with the discredited crystal activation to quantify the deformation of metals. Such a theory requires all the slip systems to obey Schmid's law and normally uses the critical resolved shear stress (CRSS) as state variable for each slip system

(Roters et al., 2010). For bulk crystals, the crystal plasticity theory mostly assumes a homogeneous dislocation structure (the identical initial CRSS). Hence most shear slips occur predominantly on the slip system with the highest Schmid factor, particularly for the single-slip deformation. However, as the specimen size decreases, this may cause a non-homogeneous distribution of dislocation configurations, and thus may lead to different initial CRSS for different slip systems. In such cases, most shear slips that occur predominantly on the slip system with the highest Schmid factor may not be guaranteed. To account for the strain burst in such a framework, we only consider the micropillars with diameters larger than a few micrometers to facilitate the assumption of homogeneous dislocation structure in this work. For example, nickel micropillars with the diameters larger than ~10 μm would be suitable (Norfleet et al., 2008).

3.1. Foundation of crystal plasticity

The kinematics of FCC crystals described below is well-established and the detailed formulations are given in literature, see for example, Asaro and Lubarda (2006). The total deformation gradient tensor $\boldsymbol{F}$ can be decomposed into the elastic tensor $\boldsymbol{F}_e$, and the plastic tensor $\boldsymbol{F}_p$:

$$\boldsymbol{F} = \boldsymbol{F}_e \boldsymbol{F}_p \tag{7}$$

where $\boldsymbol{F}_e$ represents the rotation and stretching of the lattice, $\boldsymbol{F}_p$ represents the plastic shear of the materials that do not change the lattice orientation and spacing. The plastic part of velocity gradient $\boldsymbol{L}_p$ is defined as:

$$\boldsymbol{L}_p = \boldsymbol{F}_e \cdot \dot{\boldsymbol{F}}_p \cdot \boldsymbol{F}_p^{-1} \cdot F_e^{-1} = \sum_{\alpha=1}^{n} \dot{\gamma}_\alpha s_\alpha^* \otimes n_\alpha^* \tag{8}$$

By introducing the symmetric tensor $\boldsymbol{p}_\alpha = \frac{1}{2}(s_\alpha^* \otimes n_\alpha^* + n_\alpha^* \otimes s_\alpha^*)$ and the skew-symmetric tensor $\boldsymbol{w}_\alpha = \frac{1}{2}(s_\alpha^* \otimes n_\alpha^* - n_\alpha^* \otimes s_\alpha^*)$, the plastic stretching tensor $\dot{\boldsymbol{\varepsilon}}_p$ and the plastic spin $\dot{\boldsymbol{\omega}}_p$ can be written as:

$$\dot{\boldsymbol{\varepsilon}}_p = \sum_{\alpha=1}^{n} \dot{\gamma}_\alpha \boldsymbol{p}_\alpha, \quad \dot{\boldsymbol{\omega}}_p = \sum_{\alpha=1}^{n} \dot{\gamma}_\alpha \boldsymbol{w}_\alpha \tag{9}$$

in which $\dot{\gamma}_\alpha$ is the shear rate on the αth slip system.

The constitutive equation is specified by

$$\hat{\boldsymbol{\sigma}} = \boldsymbol{\Lambda} : \dot{\boldsymbol{\varepsilon}} - \sum_{\alpha=1}^{n} \boldsymbol{\Gamma}_\alpha \dot{\gamma}_\alpha \tag{10}$$

in which $\hat{\boldsymbol{\sigma}}$ is the Jaumann stress rate and

$$\boldsymbol{\Gamma}_\alpha = \boldsymbol{C} : \boldsymbol{p}_\alpha + \boldsymbol{w}_\alpha \cdot \boldsymbol{\sigma} - \boldsymbol{\sigma} \cdot \boldsymbol{w}_\alpha, \quad \Lambda_{ijmn} = C_{ijmn} - \sigma_{ij}\delta_{mn} \tag{11}$$

where $\boldsymbol{C}$ is the tensor of the elastic modulus and $\boldsymbol{\sigma}$ is the Cauchy stress. A more detailed description of the crystal plasticity constitutive model can be found in Peirce et al. (1983).

3.2. Hardening laws in FCC pillars

We first study the deformation process within the burst slip. There is considerable debate on the origin of the burst slip. One view is that the burst activity is caused by the continuous operation of a few dislocation sources, featuring with a dislocation starvation state after each burst activity (Greer and Nix, 2006; Shan et al., 2008). Another view suggests that the origin of the burst activity is the destruction of jammed dislocation configurations (Csikor et al., 2007). Furthermore, such processes show no significant change in the dislocation density and retain the dislocation network after each burst (Csikor et al., 2007; Norfleet et al., 2008). Normally, the former mechanism possibly operates for small nanopillars associated with cataclysmic bursts, in contrast to the later mechanisms that dominates in specimens of larger sizes, featuring with small burst sizes but high frequency (Ngan and Ng, 2010; Wang et al., 2012). Therefore, for micropillars with diameters larger than a few micrometers as investigated in this work, the burst slip is expected to be attributed to the destruction of jammed dislocation configurations (Wang et al., 2012). Within the burst slip, some features of plastic deformation are described as follows:

(i) For larger specimens, the discrete slip bands are found to be distributed widely along their gauge lengths in some experiments (Dimiduk et al., 2005). These slip bands are always associated with the appearance of burst activities (Schwerdtfeger et al., 2010), suggesting that one burst activity occurs mainly in single slip systems (Csikor et al., 2007). Thus, we define the resolved shear stress τ_α for driving the fast gliding dislocations on the αth slip system, and accordingly, the current resistant strength g_α for the avalanche-like motion of dislocations, respectively.

(ii) The burst deformation is assumed to be viscous. Thus, the shear rate $\dot{\gamma}_\alpha$ on the αth slip system, is derived using a visco-plastic power-law expression (Hutchinson, 1976) as

$$\dot{\gamma}_\alpha^b = \dot{\gamma}_0 \mathrm{sgn}\left(\frac{\tau_\alpha}{g_\alpha}\right)\left(\frac{\tau_\alpha}{g_\alpha}\right)^{1/m} \tag{12}$$

where m is the rate sensitivity exponent and $\dot{\gamma}_0$ is the shear rate at a reference condition. This power-law rate equation provides us with an opportunity to investigate the strain-rate sensitivity emerging in micropillar plasticity since it is reported that strain-rate sensitivity maintains similar trends in strength with micropillar size (Jennings et al., 2011).

(iii) To be ready for the next burst event, the burst activity is observed to be associated with the reconstruction of the jammed networks (Wang et al., 2012), which involves dislocations mutually trapping each other in the context of larger dislocation tangling volumes among multiple slip systems, stable dislocation junction ensemble etc. Such processes may lead to natural strain hardening and could in turn suppress the current burst activity. Therefore, this strain hardening processes are responsible for the current resistant strength $g_{(\alpha)}$ for the avalanche-like motion of dislocations and could be described in term of the evolution of $g_{(\alpha)}$, which is written as:

$$\dot{g}_\alpha^b = \sum_{\alpha=1}^{n} h_{\alpha\beta} \left|\dot{\gamma}_\beta^b\right| \tag{13}$$

where $h_{\alpha\beta}$ is the hardening matrix and the sum includes all activated slip systems. The diagonal components $h_{\alpha\alpha}$ and the off-diagonal components $h_{\alpha\beta}$ represent the self-hardening and latent-hardening effects, respectively. Accordingly, the fast moving dislocation under the action of the resolved shear stress τ_α is obtained by the Schmid's law:

$$\tau_\alpha = \boldsymbol{p}_\alpha : \boldsymbol{\sigma} \tag{14}$$

For the holding stages as discussed in Section 2.3, a slower relaxation process is suggested. Compared to the larger strain rate of the burst slip, the shear rate $\dot{\gamma}_\alpha$ of the holding stage could be approximately written as:

$$\dot{\gamma}_\alpha^h \approx 0 \tag{15}$$

and the current evolution of the resistant strength g_α^h therefore becomes:

$$\dot{g}_\alpha^h \approx 0 \tag{16}$$

Combining Eq. (6) with Eq. (10), the Jaumann stress rate $\hat{\sigma}^{h}$ is obtained as:

$$\hat{\boldsymbol{\sigma}}^{h} \approx 0 \tag{17}$$

Finally, the loading stage occurs involving the motion of few dislocations compared to the burst slip, resulting in a low shear strain rate compared to the programmed strain rate, and thus increases the external load to activate the next burst slip. The strain hardening could be described by the formulations developed in literature (Peirce et al., 1983). In other words, the formulations including Eqs. (12)–(14) can also be applied to the loading stage but have different physical meanings.

For FCC metals, one commonly-used phenomenological hardening law is the Pierce–Asaro–Needleman (PAN) model suggested by Pierce, Asaro and Needleman. In this model, the hardening matrix $h_{\alpha\beta}$ takes the form:

$$h_{\alpha\beta} = qh_{\alpha\alpha},\ h_{\alpha\alpha} = h_0 \operatorname{sech}^2\left|\frac{h_0\gamma}{\tau_s - \tau_0}\right|,\quad \gamma = \sum_{\alpha=1}^{n}\int_0^t |\dot{\gamma}_\alpha| dt \tag{18}$$

where q describes the latent hardening effect, and is assumed to be 1.0 for coplanar and 1.4 for non-coplanar slip systems (Asaro and Needleman, 1985). h_0 is the initial hardening modulus, τ_0 is the initial value of the CRSS, and τ_s is the saturated shear stress at stage I. A number of experimental compression tests on micropillars have found that their stress–strain curves appear to remain in the easy glide stage throughout the tests (Dimiduk et al., 2005; Greer and Nix, 2006; Uchic et al., 2004), and this is indeed supported by the observation of Post-mortem Transmission Electron Microscopy (TEM) of [269] nickel specimens (Norfleet et al., 2008). It thus appears appropriate to use the PAN model to characterize the experimental stress–strain curve.

3.3. Accounting for strain burst

To consider the strain burst, we first separate the burst slip from the loading stage by considering a small dimensionless constant. This is similar to the work of Papanikolaou et al. (2012) who also introduced a dimensionless constant to separate the burst slip from the slow relaxations (comparable to the holding stage). Then, we judge the occurrence of the strain burst through the load serrations. This is similar to 3D-DDS methods, where the burst slips are judged by the load drops when the specimen plastic displacement rate was lower than the applied rate at a given time step.

3.3.1. Separation of burst slip and loading stage

Fig. 2 shows the typical schematic diagram of the history of strain rate in the loading stage, burst slip and holding stage. The burst slip occurs with a jump strain rate $\dot{\gamma}_\alpha^{b}(t^+)$ from the $\dot{\gamma}_\alpha^{l}(t^-)$ evolving in the loading stage that begins at time $t-\Delta t^{l}$ with a strain rate of $\dot{\gamma}_\alpha(t-\Delta t^{l})$. Such an event ends up with a strain rate of $\dot{\gamma}_\alpha(t+\Delta t^{b})$ truncated by a constant threshold $\dot{\gamma}_{th}$ as a definition of active time step Δt^{b}. After this, the holding stage occurs associated with zero shear rate in an idealized situation as described by Eq. (15). It should be mentioned that $\dot{\gamma}_\alpha(t+\Delta t^{b}+\Delta t^{h})$ can represent either the beginning of the loading stage or the burst slip as suggested later.

For the loading stage, the shear strain increment $\Delta\gamma^{l}$ is calculated through

$$\Delta\gamma^{l} = \dot{\bar{\gamma}}_\alpha^{l}\cdot\Delta t^{l} = \int_{\Delta t^{l}}\dot{\gamma}_\alpha(t)dt \tag{19}$$

Considering the shear rate jumps at time t, we also define:

$$\Delta\gamma(\xi) = \left[(1-\xi)\dot{\gamma}_\alpha(t-\Delta t^{l}) + \xi\dot{\gamma}_\alpha(t^+)\right]\Delta t^{l} \tag{20}$$

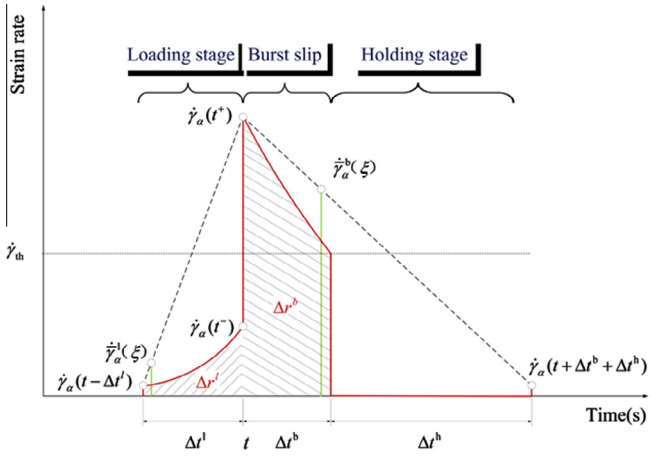

Fig. 2. Schematic description of the history of strain rate in the loading stage, burst slip and holding stage (red lines). Green lines represent the average strain rate $\dot{\bar{\gamma}}_\alpha$ that is computed using Δr (shadow area). (For interpretation of the references to color in this figure legend, the reader is referred to the web version of this article.)

Here ξ is a dimensionless parameter. $\dot{\gamma}_\alpha(t-\Delta t^{l})$ can reach $\dot{\gamma}_\alpha(t^+)$ along the path described by Eq. (12), which is different from the path that $\dot{\gamma}_\alpha(t-\Delta t^{l})$ reaches $\dot{\gamma}_\alpha(t^-)$ (red line).

As seen in Fig. 2, $\Delta\gamma^{l}$ described by Eq. (19) satisfies: $\Delta\gamma(0) < \Delta\gamma^{l} < \Delta\gamma(1)$. Hence the expression of $\Delta\gamma^{l}$ could be rewritten as:

$$\Delta\gamma^{1} = \dot{\bar{\gamma}}_\alpha^{1}(\xi)\cdot\Delta t^{1} = \left[(1-\xi)\dot{\gamma}_\alpha(t-\Delta t^{1}) + \xi\dot{\gamma}_\alpha(t^+)\right]\Delta t^{1} \tag{21}$$

by adjusting the value of $\xi \in (0,1)$. As is frequently observed in micropillar compression tests (Uchic et al., 2004; Greer and Nix, 2006), this stage always induces a nearly elastic loading within Δt^{l}, indicating a much smaller value of $\Delta\gamma^{l}$, and thus requires a comparatively small value of ξ due to the high jump strain rate of $\dot{\gamma}_\alpha(t^+)$ (the variables at initial time $t-\Delta t^{l}$ are known). In turn, when the value of $\Delta\gamma^{l}$ becomes small, we could expect a higher jump rate at the end of the loading stage by considering such a small value of ξ.The burst slip is studied by integrating it with the holding stage. Following the same approach as for the loading stage, we obtain the shear strain increment $\Delta\gamma^{b}$ by

$$\Delta\gamma^{b} = \dot{\bar{\gamma}}_\alpha^{b}(\xi)\cdot\Delta t^{b} = \left[(1-\xi)\dot{\gamma}_\alpha(t^+) + \xi\dot{\gamma}_\alpha(t+\Delta t^{b}+\Delta t^{h})\right]\Delta t^{b} \tag{22}$$

Here, ξ is obtained from the loading stage. Normally, the burst activity is characterized by a higher strain rate and larger strain increment $\Delta\gamma^{b}$ than the loading stage. On one hand, when the burst displacement ($\propto\Delta\gamma^{b}$) is large enough, $\dot{\gamma}_\alpha(t+\Delta t^{b}+\Delta t^{h})$ possibly represents an initial jump rate of the burst slip (the variable $\dot{\gamma}_\alpha(t^+)$ at initial time t are known), suggesting a succession of additional displacement events, as frequently observed in many tests. On the other hand, if $\Delta\gamma^{b}$ is featured with a moderate bust size, $\dot{\gamma}_\alpha(t+\Delta t^{b}+\Delta t^{h})$ possibly represents a negligible strain rate of the loading stage due to the viscous deformation as assumed in the loading stage. This is the case since the stain bursts are frequently observed to be separated by the loading stage in micro-compression tests. Thus, the smaller value of ξ derived from the loading stage, could be also applied to the strain burst process consisting of burst slip and holding stage.

For simplicity, we assume that ξ is a dimensionless constant. Considering Eqs. (21) and (22), the general formulation of the average shear increment rate $\dot{\bar{\gamma}}_\alpha$ can be written as:

$$\dot{\bar{\gamma}}_\alpha(\xi) = (1-\xi)\dot{\gamma}_\alpha(t) + \xi\dot{\gamma}_\alpha(t+\Delta t^{+}) \tag{23}$$

Here, the superscript + is marked to distinguish the different strain rate at time $t+\Delta t$. For example, when a loading stage evolves into

the burst slip, $\dot{\gamma}_\alpha(t+\Delta t^+)$ represents the initial jump rate of this burst activity, while $\dot{\gamma}_\alpha(t+\Delta t^-)$ suggests the strain rate at the end of the loading stage. In other words, the strain rate $\dot{\gamma}_\alpha(t+\Delta t)$ jumps from $\dot{\gamma}_\alpha(t+\Delta t^-)$ to $\dot{\gamma}_\alpha(t+\Delta t^+)$ at the time $t+\Delta t$. On the other hand, despite the expression of average shear rate being similar to that in the form of liner interpolation, it is derived theoretically for the purpose of separating the burst slip from loading stage rather than for numerical convergence.

In summary, a smaller value of ξ can lead to a fast strain rate in the burst slip compared to the loading stage, and thus separates the two processes. Additionally, when such two processes evolve into each other, the resulting strain rate fluctuations can render the load serrations due to the constant strain rate programmed by the nanoindentation system.

3.3.2. Burst slip judgment

Since the loading stage sustains an increasing load as described in Section 2.1, the produced engineering stress satisfies:

$$\dot{\Sigma}^{\mathrm{l}} \cdot \Sigma^{\mathrm{l}}(t) > 0 \tag{24}$$

In contrast, an occurrence of burst slip satisfies:

$$\dot{\Sigma}^{\mathrm{l}} \cdot \Sigma^{\mathrm{l}}(t) \leqslant 0 \tag{25}$$

where $\dot{\Sigma}^{\mathrm{l}}$ could be related with the rate of stress with:

$$\dot{\Sigma}^{\mathrm{l}} = \langle \dot{\sigma}^{\mathrm{l}} \rangle = \frac{1}{V}\int_V \dot{\sigma}^{\mathrm{l}} \mathrm{d}v \tag{26}$$

Here $\langle\cdot\rangle$ is defined by $\langle\cdot\rangle = X^{-1}\int_x \int_X \cdot\, dX$, which represents the average of a field in X, and V is the current volume.

3.4. Incremental constitutive model

For the loading stage, we assume that all the variables at time t are known and the whole process lasts for a time interval Δt^{l}. By integrating Eq. (10) from time t to $t+\Delta t$, the incremental constitutive relation becomes:

$$\Delta\boldsymbol{\sigma}^{\mathrm{l}}(\Delta t) = \boldsymbol{\Lambda} : \Delta\boldsymbol{\varepsilon}(\Delta t) - \sum_{\alpha=1}^{n}\boldsymbol{\Gamma}_\alpha \Delta\gamma_\alpha(\Delta t), \quad \Delta t \in [0, \Delta t^{\mathrm{l}}] \tag{27}$$

where the magnitudes of the stress increments $\Delta\sigma^{\mathrm{l}}$ are functions of the time increment Δt. For a given displacement increment $\Delta u^{\mathrm{l}} = -\Delta E^{\mathrm{l}} \cdot L$, using Eq. (1), the time increment Δt^{l} in Eq. (27), can be computed as

$$\Delta t^{\mathrm{l}} = \Delta E^{\mathrm{l}}/\dot{\varepsilon}_0 \tag{28}$$

For the bust slip, we examine the process in a quasi-static manner. A global burst slip occurs whenever Eq. (25) is fulfilled. Following the same approach as that for the loading stage, the incremental constitutive relation is given directly by

$$\Delta\boldsymbol{\sigma}^{\mathrm{b}}(\Delta t) = \boldsymbol{\Lambda} : \delta\boldsymbol{\varepsilon}(\Delta t) - \sum_{\alpha=1}^{n}\boldsymbol{\Gamma}_\alpha \Delta\gamma_\alpha(\Delta t), \Delta t \in [0, \Delta t^{\mathrm{b}}] \tag{29}$$

in which, $\delta\boldsymbol{\varepsilon}$ is the local strain increment produced by the global strain burst δE.

Unlike the loading stage, the relationship between the event duration Δt^{b} and the strain burst δE is unknown. That means that the time increment Δt cannot be determined directly for a given incremental displacement, thus an extra unknown parameter for determining the stress components is introduced.

For the holding stage, the incremental constitutive relation gives:

$$\Delta\boldsymbol{\sigma}^{\mathrm{h}}(\Delta t) = \mathbf{0}, \quad \Delta t \in [0, \Delta t^{\mathrm{h}}] \tag{30}$$

Here, the holding time increment Δt^{h} is also undetermined.

Considering these two problems, we fix the value of time increment Δt, which is specified by

$$\Delta t = \Delta t^{\mathrm{b}} + \Delta t^{\mathrm{h}} \tag{31}$$

Suppose that all the variables at time t are known. By integrating the rate of Cauchy stress $\hat{\sigma}$ from time t to $t+\Delta t$, the incremental constitutive relation gives:

$$\begin{aligned}\Delta\boldsymbol{\sigma}^{\mathrm{b+h}} &= \int_t^{t+\Delta t}\hat{\boldsymbol{\sigma}}dt = \int_t^{t+\Delta t^{\mathrm{b}}}\left(\Lambda : \delta\dot{\varepsilon} - \sum_{\alpha=1}^{n}\boldsymbol{\Gamma}_\alpha\dot{\gamma}_\alpha\right)dt \\ &= \boldsymbol{\Lambda} : \delta\boldsymbol{\varepsilon}(\Delta t^{\mathrm{b}}) - \sum_{\alpha=1}^{n}\boldsymbol{\Gamma}_\alpha\Delta\gamma_\alpha(\Delta t^{\mathrm{b}})\end{aligned} \tag{32}$$

Here, superscript b + h represent the stress increments within the total time of the burst duration Δt^{b} and the holding time Δt^{h}.

As shown in Fig. 1(b), during the fixed time increment Δt, the magnitude of the nanoindentation loading displacement increment Δu is equal to that of the displacement burst δu within the burst duration Δt^{b}. Thus, the following relation holds:

$$\Delta u(\Delta t) = \delta u(\Delta t^{\mathrm{b}}) \tag{33}$$

where

$$\Delta u(\Delta t) = L \cdot \dot{\varepsilon}_0 \cdot \Delta t \tag{34}$$

$$\delta u(\Delta t^{\mathrm{b}}) = L \cdot \delta\dot{\varepsilon} \cdot \Delta t^{\mathrm{b}} \tag{35}$$

Here, $\delta\dot{\varepsilon}$ is the burst slip rate within the burst event duration Δt^{b}.

Taking into account the uniqueness theorems of solutions, the local strain increment induced by δu is equal to that of Δu, and thus the first term of the right-hand side in Eq. (32) can be replaced by

$$\boldsymbol{\Lambda} : \delta\boldsymbol{\varepsilon}(\Delta t^{\mathrm{b}}) = \boldsymbol{\Lambda} : \Delta\boldsymbol{\varepsilon}(\Delta t) \tag{36}$$

Then, following Eq. (32), an alternative constitutive relation is obtained as:

$$\Delta\boldsymbol{\sigma}^{\mathrm{b+h}}(\Delta t; \Delta t^{\mathrm{b}}) = \boldsymbol{\Lambda} : \Delta\boldsymbol{\varepsilon}(\Delta t) - \sum_{\alpha=1}^{n}\boldsymbol{\Gamma}_\alpha\Delta\gamma_\alpha(\Delta t^{\mathrm{b}}) \tag{37}$$

in which the stress increments $\Delta\boldsymbol{\sigma}^{\mathrm{b+h}}(\Delta t; \Delta t^{\mathrm{b}})$ are dependent on both fixed time increment Δt and burst duration Δt^{b}.

For a displacement burst $\delta u = L \cdot \delta E$, combining Eqs. (33) and (34) gives the fixed time increment Δt

$$\Delta t = \delta E/\dot{\varepsilon}_0 \tag{38}$$

where the amplitude of δE satisfies the statistical distribution prescribed by Eq. (4). The method of determining the event duration Δt^{b} is given in the appendix.

In summary, we can propose a constitutive model that describes the intermittent plastic flow in the form of a piecewise function as follows:

$$\boldsymbol{\Delta\sigma} = \begin{cases} l\boldsymbol{\Lambda} : \boldsymbol{\Delta\varepsilon}(\Delta t) - \sum_{\alpha=1}^{n}\boldsymbol{\Gamma}_\alpha\Delta\gamma_\alpha(\Delta t); & \text{When } \ \Delta S_{\mathrm{l}} \cdot S_{\mathrm{l}}(t) > 0 \ (a) \\ \boldsymbol{\Lambda} : \boldsymbol{\Delta\varepsilon}(\Delta t) - \sum_{\alpha=1}^{n}\boldsymbol{\Gamma}_\alpha\Delta\gamma_\alpha(\Delta t^{b}); & \text{When } \ \Delta S_{\mathrm{l}} \cdot S_{\mathrm{l}}(t) \leqslant 0 \ (b) \end{cases} \tag{39}$$

4. Finite element implementation

4.1. Amplitude of strain burst

Considering Eq. (4), one may note that as the burst size asymptotically approaches zero, the value of $p(\delta E)$ diverges. That is, only the amplitudes above the lower limit $\delta E_{\min}$ follow the power-law behavior. Such lower limit usually corresponds not to the smallest

value of the strain bursts observed from experimental data. In practice, there are some other non-power-law behaviors below $\delta E_{\min}$ (Brinckmann et al., 2008; Dimiduk et al., 2010). In the present work, we only take into consideration, the strain bursts that satisfy the statistical distribution described by Eq. (4), while those with amplitude below $\delta E_{\min}$ are incorporated into the loading stage since they are negligibly small in value. Accordingly, $\delta E_{\min}$ is expressed by (Zhang et al., 2012)

$$\delta E_{\min} = 4b/L \tag{40}$$

where b is the Burgers vector.

The largest magnitude $\delta E_{\max}$ is expressed (Csikor et al., 2007; Devincre and Kubin, 2010) as:

$$\delta E_{\max} = \frac{bE}{L(\theta + \Gamma)} \tag{41}$$

Here, E, θ and Γ are the elastic modulus, the constant strain hardening coefficient and the effective stiffness of the load-machine, respectively.

It should be mentioned that the present work mainly focuses on the continuum model to capture the strain burst, an accurate description of the strain burst behavior is not essential. Thus, we set the stochastic nature of the strain burst aside in the finite element analysis.

4.2. Time increment

The time increment Δt in Eq. (38) is determined by δE, which is limited by the characteristic size of the specimen. This implies that the value of Δt is also size dependent. Following Eq. (38), the range of Δt satisfies:

$$\delta E_{\min}/\dot{\varepsilon}_0 \leqslant \Delta t \leqslant \delta E_{\max}/\dot{\varepsilon}_0 \tag{42}$$

As a consequence, the time steps in the finite element calculations are within the above range, associated with $\Delta t_{\min} = \delta E_{\min}/\dot{\varepsilon}_0$ and $\Delta t_{\max} = \delta E_{\max}/\dot{\varepsilon}_0$. However, one problem exists. During the finite element calculations, the magnitude of time step Δt quickly increases to $\Delta t_{\max}$ and then remains invariant, due to a good convergence property and stability of the algorithm. As a result, the strain bursts with the largest amplitude are mostly captured. However, for a fixed total strain, this could lead to only a few strain bursts being captured in the calculations, and is also contradictory to the actual experiment tests where the probability that the strain burst occurs with the amplitude of $\delta E_{\max}$ is small. To solve this problem, we can reasonably take

$$\Delta t_{\max} = \delta \bar{E}/\dot{\varepsilon}_0 \tag{43}$$

in which, $\delta \bar{E}$ is the average burst size, and is computed by

$$\delta \bar{E} = \int_{\delta E_{\min}}^{\delta E_{\max}} E \cdot p(E) dE \tag{44}$$

The reason to take $\Delta t_{\max} = \delta \bar{E}/\dot{\varepsilon}_0$ arises from the following considerations. (i) As described in Eqs. (40) and (41), $\delta E_{\min}$ and $\delta E_{\max}$ are all limited by the specimen size L. This means that $\delta \bar{E}$ is also size dependent ($\delta \bar{E} \propto 1/L$) and the time increment Δt computed by Eq. (43) is ultimately limited by the characteristic specimen size. (ii) For better illustration, we show the relationship between the average amplitude of $\delta \bar{E}$ and $\delta E_{\max}$ in Fig. 3(a). We find that the variation of $\delta \bar{E}$ has the same trend as that of $\delta E_{\max}$. (iii) The probability of δE that falls in the range $\delta E_{\min} \sim \delta \bar{E}$ is calculated by

$$P(\delta E_{\min} \leqslant \delta E \leqslant \delta \bar{E}) = \int_{\delta E_{\min}}^{\delta \bar{E}} p(E) dE \tag{45}$$

Fig. 3(b) shows that the value of P is a function of $\delta E_{\max}$ (scaled by b/L). It is seen that P generally satisfies $P \geqslant 50\%$. When $L\delta E_{\max}/b \geqslant 1000$, the probability P almost reaches 80%. This means that most of burst sizes fall in the range $\delta E_{\min} \sim \delta \bar{E}$. These burst sizes are sufficient in employing our continuum model to take the strain bursts into account.

4.3. Implementation of the algorithm into finite element analysis

We perform finite element analysis using the user material interface (UMAT) in the commercial code ABAQUS/Standard (2009). In the finite element analysis, the equations must be discretized in order to solve the boundary value problems incrementally. The global engineering stress increment $\Delta\Sigma$ are rewritten as the following weighted sum form

$$\Delta\Sigma(\Delta t) = \frac{1}{V}\sum_{ipn=1}^{N_{ipn}} [\Delta\boldsymbol{\sigma}_{ipn}(\Delta t)\cdot\boldsymbol{n}] w_{ipn} J_{ipn} \tag{46}$$

where ipn is the integration point number, N_{ipn} is the total number of integration points, w_{ipn} and J_{ipn} are the weight and Jacobi matrix of integration point ipn, respectively.

The burst duration Δt^{b} is determined using a bisection method. The value of Δt^{b} is accepted when the value of $\Delta\Sigma^{\mathrm{b+h}}(\Delta t; \Delta t^{\mathrm{b}})$ is smaller than a specified tolerance$e$:

$$|\Delta\Sigma^{\mathrm{b+h}}(\Delta t; \Delta t^{\mathrm{b}})| \leqslant e \tag{47}$$

The tolerance e is calculated by

$$e = 5\%\tau_0 \delta E_{\min}/EM \tag{48}$$

where E is the total engineering strain and M is the Schmid factor. Here, Eq. (48) can ensure that the relative error of the calculated results of Σ is less than 5%, at a total engineering strain E.

The shear strain increment $\Delta\bar{\gamma}_\alpha$ on the αth slip system is computed by

$$\Delta\bar{\gamma}_\alpha(\Delta t) = \left[\dot{\gamma}_\alpha(t) + \xi\frac{\partial\dot{\gamma}_\alpha}{\partial\tau_{(\alpha)}}\Delta\tau_{(\alpha)} + \xi\frac{\partial\dot{\gamma}_\alpha}{\partial g_{(\alpha)}}\Delta g_{(\alpha)}\right]\Delta t \tag{49}$$

The above Eq. is obtained using Taylor expansions through the path that $\dot{\gamma}_\alpha(t - \Delta t^{\mathrm{l}})$ reaches $\dot{\gamma}_\alpha(t^+)$ by Eq. (12). Thus, the updated variables such as $\dot{\gamma}_\alpha(t)$ at time t represent the initial state of the next increment such as burst slip ($\dot{\gamma}_\alpha(t^+)$), rather than the end state of the last increment such as loading stage ($\dot{\gamma}_\alpha(t^-)$).

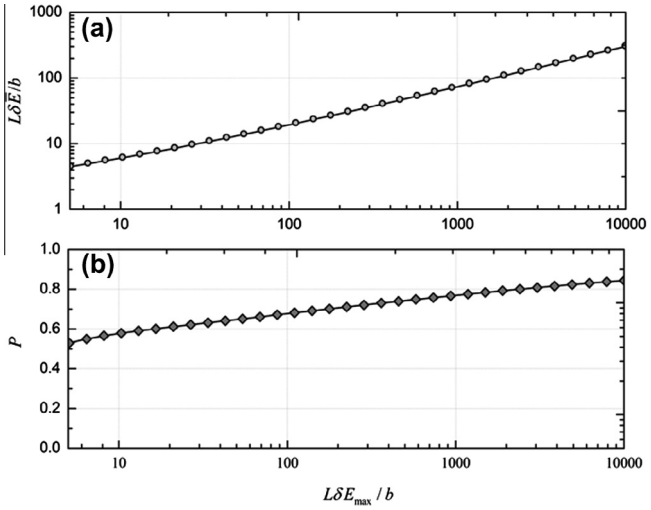

Fig. 3. (a) Average burst size $\delta\bar{E}$ (normalized by the Burgers vector b) derived by Eq. (44) as a function of the largest burst size $\delta E_{\max}$ (normalized by b). (b) Probability P derived by Eq. (45) as a function of $\delta E_{\max}$ (normalized by b).

Some other formulations in the UMAT follow that of Asaro (1983a,b). The essential steps in the UMAT update algorithm are described in Fig. 4.

4.4. Verification of the algorithm

In order to check the correctness of the implementation and the accuracy of the proposed present model, we first compare the present model, against the crystal-plasticity finite element method (CPFEM) using a UMAT for single-crystal plasticity that was written by Huang (1991) and later revised by Kysar (1997). As the mechanical behavior of bulk single crystals of pure nickel having a [269] orientation has been reported in Dimiduk et al. (2005), we consider the compression tests of bulk single-crystal nickel having dimensions of $1 \times 1 \times 1$ mm, and select the sample deforming under nominally single slip with a [269] orientation in the simulations mainly for the sake of determining the hardening parameters and for comparison purpose as well. For simplicity, the finite element model consists of a single 8-node brick-type element (C3D8). The displacements are applied along the y-direction associated with a constant strain rate of 1.0×10^{-4}/s. The stress-free boundary conditions are prescribed on the x–y and y–z planes. Further details on the finite element models are shown in Fig. 5.

Table 1 summarizes the hardening parameters required in both the CPFEM and present models. The elastic constants are chosen to be c_{11} = 246.5 GPa, c_{12} = 147.3 GPa and c_{44} = 124.7 GPa, which are taken from Freund and Suresh (2003). For the additional parameters ($\delta\bar{E}$, $\delta E_{\min}$) of the present model, refer to the discussion in Section 4.1.

Fig. 6(a) compares the calculated macroscopic stress–strain curve predicted by the present model with the analogous plastic flow curve obtained from the CPFEM method. Both models predict a smooth macroscopic curve that is consistent with that obtained by Uchic et al. (2004) and Dimiduk et al. (2005) in the compression tests of macro-samples, and a good agreement between two models is evident from the Fig. 6(a). However, a large number of the staircase-like steps were detected in the present model (see Fig. 6(b)) and they are verified to be the strain burst, as discussed later. These tiny steps for macrosample deformation are very difficult to detect by experimental tools and are also rarely revealed from the numerical simulations such as 3D-DDS.

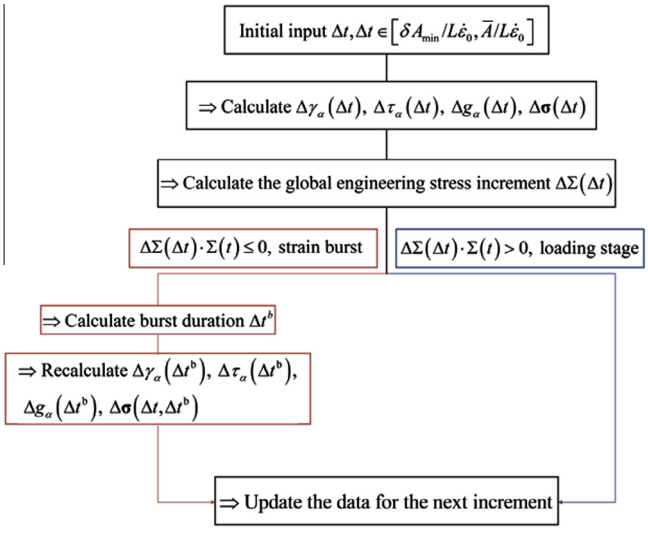

Fig. 4. The solution procedure of present model.

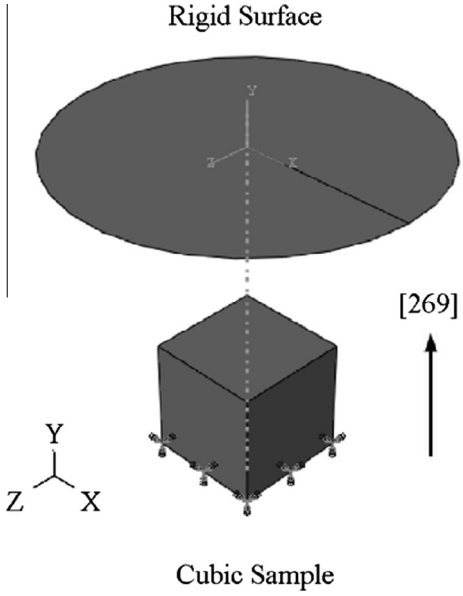

Fig. 5. Finite element model for [269] cubic sample with boundary conditions. The load on the sample is applied by the rigid surface. The [269] orientation is parallel to the y-direction.

Table 1
Hardening parameters for both the CPFEM and present model.

τ_0	τ_s	h_0	m	$\dot{\gamma}_0$
17.5 MPa	26.7 MPa	61.8 MPa	0.0005	0.001 s^{-1}

5. Simulation of Ni micropillar compression test: results

The mechanical behavior of typical FCC metal Ni has been experimentally investigated by many researchers. These studies demonstrate that the micropillars, 18–40 μm in diameter, show a Stage I easy-glide mode of deformation throughout the compression tests (Dimiduk et al., 2005), and the Schmid law still holds for the micropillars with diameters larger than ~10 μm (Norfleet et al., 2008). In the present study, we are interested in the flow intermittency under conditions of HLM and three-dimensional finite element simulations are performed. We simulate nickel micropillars with diameters of ~20 and ~30 μm, as well as bulk crystals having diameter of ~3 mm, for comparison with the results of Dimiduk et al., 2005, 2006.

5.1. Finite element model characteristics in nickel micropillars

Fig. 7 shows the geometric details of the model used in the analysis of ~20 μm micropillar. This configuration is roughly equivalent to that of the actual micro-compression testing samples (Dimiduk et al., 2005, 2006). The parameters of the configuration are chosen according to the suggestions of Choi et al. (2007). The boundary conditions used in our simulations mimic the experimental conditions with the displacements prescribed along the y-direction and the bottom of substrate being fixed. The loading is performed by a rigid surface representing the stiff flat diamond tip of nanoindentor. In addition, the loading axis is designed to align along the [269] single-slip direction. To imitate the loading conditions of the experiments, the loading velocity is set at a constant displacement rate of 1.0×10^{-4}/s for all the simulations, which results in quasi-static deformation of the micropillars. C3D8 type elements with full integration are used to discretize the model. Table 2 lists the model parameters assigned to the nick-

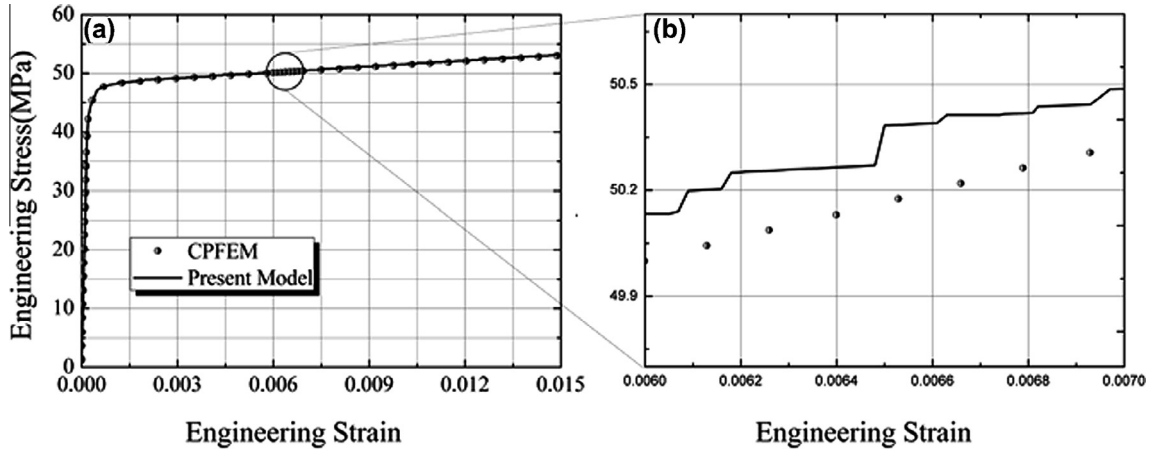

Fig. 6. Comparison of the flow stress vs. strain curves obtained from the present model and CPFEM for bulk crystal Ni. (a) Macroscopic stress–strain curve; (b) Enlarged presentation of a portion of the curve. The scattered circle and solid lines represent the results from present model and CPFEM, respectively.

el micropillar samples with diameters of ~20 and ~30 μm as well as bulk nickel crystal, respectively.

5.2. Verification of strain burst

As discussed in Section 3.2, the burst slip can be attributed to the destruction of jammed dislocation configurations. Such one-burst activity occurs mainly in single slip system in relation to the collective, avalanche-like motion of dislocations, and thus leads to higher strain rate, which is described by Eq. (12). Hence, when the calculated strain rate in single slip system from the theoretical model is larger than the programmed rate at a given time step, a strain burst occurs.

To illustrate the high strain rate of the strain burst, the shear stress as function of time for the ~20 μm Ni micropillar is plotted in Fig. 8; the inset shows one of the portions of the shear stress and the average velocity as functions of time as an example. It is seen that as the plastic deformation proceeds, some staircase-like sections (shear stress plateau) emerge. In these sections, the corresponding average velocities of micropillar all exceed those pre-programmed (v_p = 4.7 nm/s) by the nanoindentation system (see the inset in Fig. 8) and thus indicates a higher strain rate than the programmed constant strain rate. Such phenomenon is commonly identified as a strain burst in the micropillar tests. Additionally, we also see that the velocities become zero in certain time sections. This occurs only at the end of each burst event, and represents a holding stage.

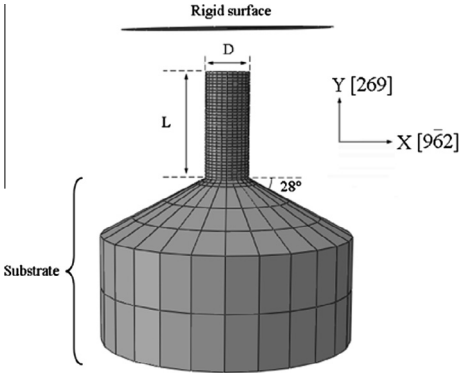

Fig. 7. Finite element model for the micropillar of ~20 μm in diameter. D and L represent the pillar diameter and length, respectively.

Table 2
The simulation parameters for the samples.

D (μm)	τ_0 (MPa)	τ_s (MPa)	h_0 (MPa)	m	$\delta\bar{E}$	δE_{min}
~3000	19	40	32	0.001	2.5×10^{-6}	1.4×10^{-7}
~30	25	31	38	0.03	2.5×10^{-4}	1.1×10^{-5}
~20	26	33	60	0.05	3.8×10^{-4}	2.0×10^{-5}

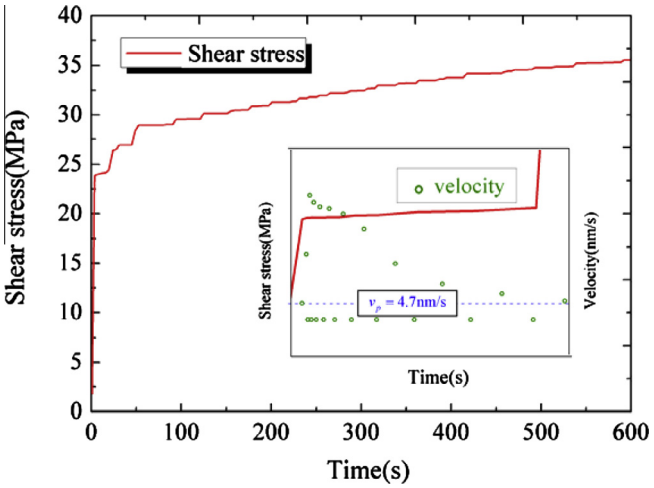

Fig. 8. The shear stress as function of time for the ~20 μm Ni micropillar during loading process. Inset: portion of the shear stress and velocity vs. time curves. v_p represents the pre-programmed strain rate by nanoindentation system.

5.3. Stress–strain response

Fig. 9 shows the calculated uniaxial macro stress–strain curves for nickel micropillars with diameters of ~20 and ~30 μm, compared with the typical experimental stress–strain curves of Dimiduk et al. (2005, 2006). The stress–strain curve of bulk crystal having dimensions of 3 × 3 × 7.4 mm is also shown in this figure. For both simulations and experiments on ~20 and ~30 μm nickel micropillars, one may observe that the plastic flow proceeds by small repeated strain bursts, which are visible as steps on the stress–strain curves. These strain bursts occurs associated with constant stress. As expected from the piecewise nature of the constitutive model, the strain bursts are separated by increments of

nearly elastic loading stages, thus giving rise to the staircase-like shape. This is in contrast to the bulk crystal that shows an apparently smooth plastic deformation (see Fig. 9), which actually consists of many tiny strain bursts. Additionally, the PAN model matches the experimentally measured stress–strain plastic flow curves to a good extent, by using the fitted model parameters listed in Table 2.

It should be mentioned that the initial loading part of the simulation curves indicates a rather large value of the elastic modulus, compared to that obtained from experiments. Many experiments have reported that, the initial part of the experimental stress–strain curve appears to be compliant during the loading process. Dimiduk et al. (2005) argued that, the under-estimation of the elastic modulus can be rationalized by the misalignment between the nanoindentation surface and the specimens, because it is difficult to ensure perfect alignment between them during the micropillar tests. Greer and Nix (2006) Suggested that the abnormally compliant loading may be caused partially by the compliance of the substrate integrated with at the bottom of the micropillar. In our calculations, we have accounted for the effect of the substrate on the micropillars rather than the bulk crystal. As shown in Fig. 9, the initial elastic responses of both micropillars and bulk crystal appear to be identical, suggesting a negligible effect of the compliance of the substrate on the under-estimation of the elastic modulus.

According to Csikor et al. (2007), the emergence of fluctuations is due to the fact that the largest amplitude of the strain bursts is increased as the sample size decreases. Fig. 10 gives an enlarged view of the calculated results of the distributions of the loading stage and the burst slip during the plastic flow, for the ~20 μm micropillar. It is seen that some of the strain bursts occur successively, and thus lead to a large "step length" (Fig. 10), as is frequently observed in many micro-compression experiments. Our results indicate that the feature of intermittent flow in micro-scale is intensified partly by the cumulative effect of a series of burst slips. As mentioned in the micropillar tests of Dimiduk et al. (2005), large "step lengths" are frequently observed in the stress–strain curves, producing the remarkable intermittent flow. These large "step lengths" should not be attributed to a single burst slip event, even if it is the occurrence of the largest burst slip. In practice, the largest amplitude of the strain burst is often associated with a small probability (Csikor et al., 2007).

5.4. Sensitivity study on the strain rate sensitivity m and the reference shearing rate $\dot{\gamma}_0$

Normally, the assumed values of m and $\dot{\gamma}_0$ from open research are not unique for a specific material. Recent study has shown that the strain burst phenomenon is sensitive to m (Jennings et al., 2011). Fig. 11 presents the effect of rate sensitivity exponent m on the stress–strain response for the microsamples that are ~20 μm in diameter. This plot shows that the smaller value of m results in much smoother plastic flow characterized by many fine stair-like steps, in contrast to those larger ones which produce pronounced flow intermittence, featuring with several larger "step length". Therefore, comparing the predicted plastic flow behaviors at different values of m to those of experimental observations, we can roughly determine the magnitudes of m for the samples as presented in Table 2.

Based on these results, we find that the value of m increases as the sample size decreases, which is in qualitative agreement with the recent atomistic simulation (Zhu et al., 2008) and experimental findings (Jennings et al., 2011). Additionally, the bulk crystal has a smaller value of m, suggesting the rate-independent plastic yield behavior on a macroscopic scale.

Fig. 12 presents the predicted stress–strain response for all microsamples under various values of the reference shearing rate, ranging from 1.0×10^{-4} to 1.0×10^{-2}. We see that the values of $\dot{\gamma}_0$ show no significant influence on the intermittent flow behavior, although the flow stress increases when $\dot{\gamma}_0$ is decreased from 1.0×10^{-2} to 1.0×10^{-4}. For specimen size investigated in this work, we take the widely used value of $\dot{\gamma}_0 = 1.0 \times 10^{-3}\ s^{-1}$ for all the simulations.

6. Discussion

The continuum model has been developed to describe the intermittent deformation behavior of micropillar samples having a single-slip orientation. As seen in Fig. 8, the predicted results could capture a series of strain bursts, producing an intermittent plastic flow. In addition, in spite of macroscopic steady rate of working hardening from the bulk crystal, we can indentify quantities of burst activities (see Fig. 6). It is found that, as the specimen size decreases, the proportion of strain bursts becomes larger and larger,

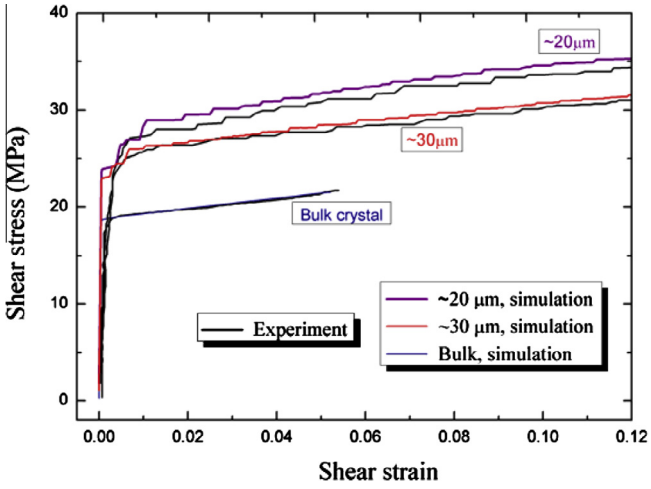

Fig. 9. Comparison of the shear stress vs. strain responses between simulations and experiments (Dimiduk et al., 2005, 2006): micro-compression tests of [269] nickel pillars with diameters of ~20 and ~30 μm as well as bulk crystal, respectively.

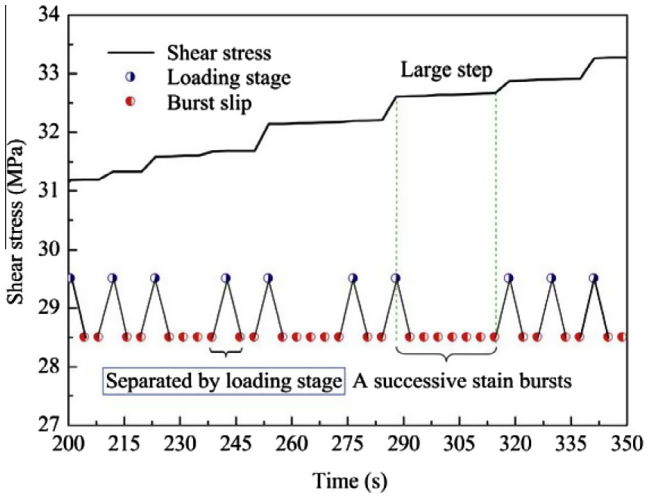

Fig. 10. Occurrence of the loading stage and the burst slip as well as shear stress as the function of the time, within one portion of the plastic flow period of ~20 μm micropillar. The blue and red circles represent the loading stage and burst slip, respectively. (For interpretation of the references to color in this figure legend, the reader is referred to the web version of this article.)

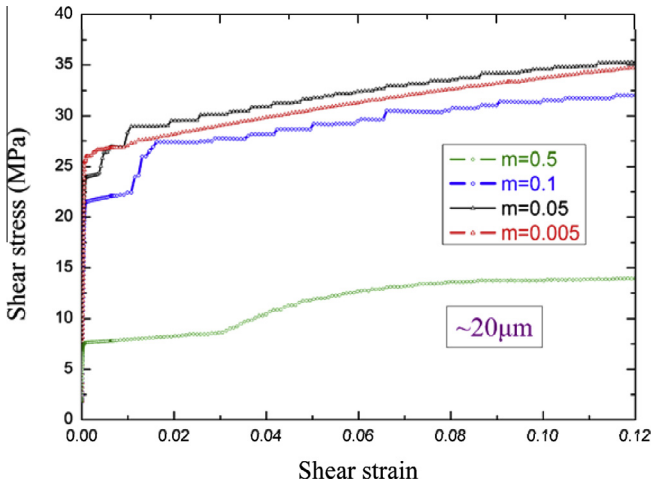

Fig. 11. Plastic flow response as a function of the strain rate sensitivity.

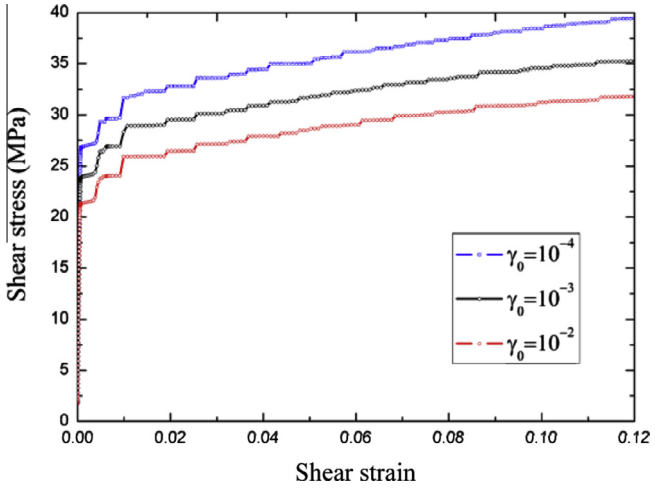

Fig. 12. Plastic flow response as a function of the reference shearing rate.

in contrast to that of the loading stage. Because of relatively smaller proportion of loading stage, a larger number of the successive strain bursts tend to occur, and this leads to larger "step length". As a result, we can see in many microcompression tests that, as the specimen decreases in size, the overall shape of the simulated flow curves exhibits severely intermittent flow that is characterized by much larger steps. Overall, the present model could reflect the change of plastic behavior from steady plastic flow for bulk crystal to intermittent plastic flow for micropillar. Although this model accounts for strain burst characteristics ($\delta E_{\min}$, $\delta\bar{E}$), the stochastic nature of the burst sizes exhibiting a power-law distribution is not represented in the simulation. Incorporating such stochastic nature into a continuum model will be discussed elsewhere, since the focus of the present work is the continuum model of capturing the strain burst.

The size-dependent effects involved in this work mainly include the flow strength, strain burst and strain-rate sensitivity. The implementation of the size dependence in the model is based on the size dependence of the averaged burst size (see Section 4.2). This model reflects two kinds of size-dependent phenomena: (i) As the specimen decreases in size, the intermittent flow becomes more pronounced (see Fig. 9). (ii) As the specimen decreases in size, the strain-rate dependence becomes stronger, as described in Section 5.4.

Size-dependent strength is one of the main issues in micropillar plasticity. Some finite element crystal plasticity models have earlier been proposed based on dislocation density considerations (Ma et al., 2006a,b,c). Such models could treat mechanical size effects in conjunction with local orientation gradients because of the introduction of the geometrically necessary dislocation densities. According to the present model, Fig. 9 shows that the flow stress increases as the sample size decreases. This is because of the material parameters used in Table 2. These parameters were obtained by resorting to the available experimental data and they are used as inputs for the simulation of intermittent flow.

For the present model, the strain bursts are assumed to originate from the destruction of jammed dislocation configurations and the produced burst rate are calculated thorough Eqs. (12)–(14). When the produced shear strain rate is larger than that applied by the nanoindentation system, a strain burst occurs. We found in our calculations that the occurrence of the strain burst (Eq. (25) is equivalent to $\Delta\Sigma^{\mathrm{I}} \geqslant 0$ for compression test) is always associated with negative values of the second-order work $d^2W_2 = \int_V \hat{\boldsymbol{\sigma}} : \boldsymbol{\varepsilon} dV \leqslant 0$ (see Fig. 13), where V is the volume of the body investigated at certain time. In other words, the negative values of the second-order work could be employed to judge the emergence of the strain burst as described in Section 3.3. It should be mentioned that, although load serration could be applied to judge the strain burst for the uniaxial deformation as commonly used in the 3D-DDS, its application may not be suitable in complex boundary problems such as microbending, 3D shear deformation. Thus, the use of the second-order work criterion seems to have certain advantages over the loading serration criterion, as a strain burst criterion. A detailed exanimation of the validity of this criterion is underway, which is beyond the scope of the present paper.

Finally, because of the negative values of the second-order work, it is suggested that the strain bursts are associated with unstable deformations. Mesh convergence is a well known difficulty in modeling material instability with finite element analyses, due to the non-convergence of solutions with increased refinement of finite element meshing. For this problem, we consider three different meshes including coarse mesh, normal mesh and refined mesh. Fig. 14 shows the predicted stress vs. strain behaviors of the ~20 μm diameter micropillar using the three different meshes. It is seen that the intermittent plastic behaviors for the three FE computations are well represented, and are not significantly affected by a refined mesh. Although the predicted intermittent

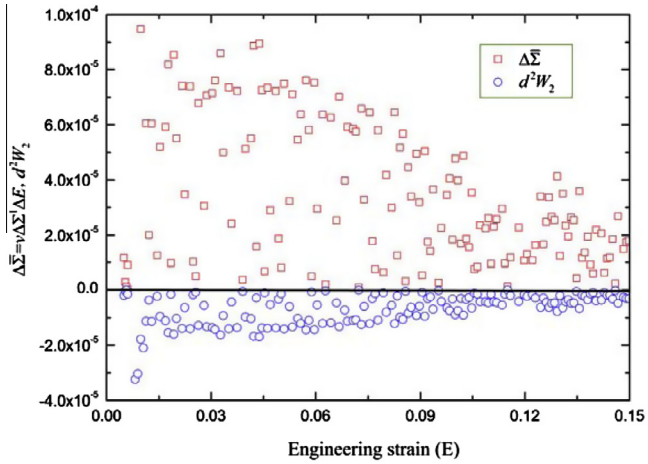

Fig. 13. The value of the second work (d^2W_2) and the engineering stress increments ($\Delta\Sigma$) as the history of total engineering strain (E) in the simulation of ~20 μm micropillar. The blue circle and red square marks represent the value of the second work and the engineering stress increments, respectively. The value of $\Delta\Sigma$ is scaled by $1/\nu\Delta E$. (For interpretation of the references to color in this figure legend, the reader is referred to the web version of this article.)

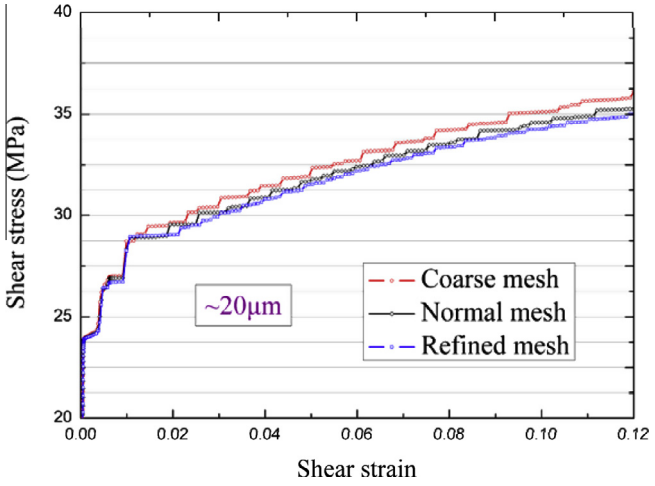

Fig. 14. Mesh convergence studies: coarse mesh (1740 elements), normal mesh (3480 elements) and refined mesh (6960 elements).

plastic behaviors are not completely identical (caused by cumulative errors) for the three different meshes, the curves shown in the plot indicate that discrepancy in the macroscopic responses is less noticed. For the bulk crystal, the results in Fig. 9 from the present model are obtained from more-element analysis (720 elements) rather than one-element simulations as shown in Fig. 6. However, the former is not very different from the latter, in terms of their plastic flow behaviors. Furthermore, the predicted results converge to that from CPFEM analysis, also suggesting the convergence and stability of the FEM algorithm.

7. Conclusion

We have formulated a continuum model accounting for the strain bursts observed in the compression tests of single crystal micropillars. We consider the intermittent space and time displaying in the displacements of pillars under the loading conditions of Dimiduk and coworkers (Dimiduk et al., 2005, 2006; Shade et al., 2012). The microscopic boundary conditions (MBCs) in this loading method (hybrid loading mode) are constructed. Such a model has been implemented into finite element analysis. To validate our model, finite element simulations of uniaxial compression tests on face-centered cubic [269] nickel micropillars are performed. The results show the following:

(1) Our simulations clearly show visible strain bursts during the plastic flow of single crystal micropillars, and the predicted behavior of the stress–strain response is qualitatively comparable with those of experimental observations (Dimiduk et al., 2005, 2006).
(2) For the bulk crystal, we could identify a series of strain bursts in the course of plastic flow.
(3) Many strain bursts occur in successively during the loading process. The more pronounced intermittent flow with decreasing specimen size could be attributed to both increasing numbers of the successive strain bursts and increasing amplitude of the strain burst (Csikor et al., 2007).
(4) The occurrence of strain burst is always associated with negative values of the second-order work, suggesting that the second-order work criterion may be applicable to burst activities in micropillar plasticity.

Furthermore, it is possible to take into account, the stochastic nature of burst size in our model (i.e. different plastic flow responses for the same diameter micropillars). However, it is beyond the scope of the present study.

The main purpose of this paper was to illustrate a continuum model in crystal plasticity that can capture a series of the strain bursts. The results incorporating such a stochastic nature in the continuum model will be discussed elsewhere, wherein this model is employed to study both the temporal aspects of the plastic flow and the mechanical response of crystalline materials in micropillar compression (Zhang and Shang, 2013).

Acknowledgments

This work was supported by NSAF through Grant No. U1330116 and National Natural Science Fund of China through Grant No. 11272243.

Appendix A. Calculation of the burst duration

The stress increments per unit volume are linked with global body by

$$\Delta\boldsymbol{\Sigma} = \langle \Delta\boldsymbol{\sigma} \rangle = \frac{1}{V}\int_V \Delta\boldsymbol{\sigma}\, \mathrm{d}v \tag{A.1}$$

Here $\langle\cdot\rangle$ is defined by $\langle\cdot\rangle = X^{-1}\int_X \cdot\, dX$, which represents the average of a field in X; and V is the current volume.

For the micro-compression tests, the engineering stress increment $\Delta\Sigma^{b+h}$ is defined within the total time of the burst duration Δt^b and the holding stage Δt^h, and is expressed by

$$\Delta\Sigma^{b+h}(\Delta t;\Delta t^b) = \Delta\boldsymbol{\Sigma}(\Delta t;\Delta t^b)\cdot\vec{\boldsymbol{n}} \tag{A.2}$$

where $\Delta\boldsymbol{\Sigma}(\Delta t;\Delta t^b) = \langle \Delta\sigma^{b+h}(\Delta t;\Delta t^b)\rangle$ and vector $\vec{\boldsymbol{n}}$ is along the pillar axis. Based on the extra force boundary condition as described in Eq. (2), the loading conditions within the fixed Δt give

$$\Delta\Sigma^{b+h}(\Delta t;\Delta t^b) = \Delta\Sigma^{b}(\Delta t^b) + \Delta\Sigma^{h}(\Delta t - \Delta t^b) = 0 \tag{A.3}$$

where $\Delta\Sigma^b$ and $\Delta\Sigma^h$ represent the engineering stress increment within the burst slip and the holding stage, respectively.

When a strain burst occurs under a compression test, the following relation should be satisfied due to the relaxation of stress:

$$\Delta\Sigma(\Delta t) = \Delta\Sigma^{b+h}(\Delta t;\Delta t) > 0 \tag{A.4}$$

but this relaxation is prevented by the nanoindentation system, thus giving rise to the fulfillment of Eq. (2), (A.4).

On the other hand, $\Delta\sigma^{b+h}(\Delta t;0)$ represents a purely elastic loading and thus gives:

$$\Delta\Sigma^{b+h}(\Delta t;0) < 0 \tag{A.5}$$

Combining Eqs. (A.5) and (A.6), the following relation holds:

$$\Delta\Sigma^{b+h}(\Delta t;0)\Delta\Sigma^{b+h}(\Delta t;\Delta t) < 0 \tag{A.6}$$

where $\Delta t^b \in [0,\Delta t]$. According to the intermediate value theorem, the solution of Eq. (A.4) indeed exists for a certain time increment Δt. By definition, Δt^b regulates the value of the burst duration, at which the engineering stress increment remains unchanged, as a consequence, its uniqueness is guaranteed.

The event duration Δt^b can be calculated through an alternative form of Eq. (A.4), as:

$$\langle \Delta\boldsymbol{\sigma}^{b+h}(\Delta t;\Delta t^b)\rangle\cdot\vec{\boldsymbol{n}} = 0 \tag{A.7}$$

References

ABAQUS, 2009. ABAQUS/Explicit User's Manual, Version 6.9. Providence, Rhode Island, USA.
Akarapu, S., Zbib, H.M., Bahr, D.F., 2010. Analysis of heterogeneous deformation and dislocation dynamics in single crystal micropillars under compression. Int. J. Plast. 26, 239–257.
Asaro, R.J., 1983a. Crystal plasticity. J. Appl. Mech. 50, 921–934.

Asaro, R.J., 1983b. Micromechanics of crystals and polycrystals. Adv. Appl. Mech. 23, 1–115.
Asaro, R.J., Lubarda, V.A., 2006. Mechanics of Solids and Materials. Cambridge University Press.
Asaro, R.J., Needleman, A., 1985. Texture development and strain hardening in rate dependent polycrystals. Acta Metall. 33, 923–953.
Brinckmann, S., Kim, J.Y., Greer, J.R., 2008. Fundamental differences in mechanical behavior between two types of crystals at the nanoscale. Phys. Rev. Lett. 100, 155502.
Choi, Y.S., Uchic, M.D., Parthasarathy, T.A., Dimiduk, D.M., 2007. Numerical study on microcompression tests of anisotropic single crystals. Scripta Mater. 57, 849–852.
Csikor, F.F., Motz, C., Weygand, D., Zaiser, M., Zapperi, S., 2007. Dislocation avalanches, strain bursts, and the problem of plastic forming at the micrometer scale. Science 318, 251–254.
Devincre, B., Kubin, L., 2010. Scale transitions in crystal plasticity by dislocation dynamics simulations. Comptes Rendus Phys. 11, 274–284.
Dimiduk, D.M., Uchic, M.D., Parthasarathy, T.A., 2005. Size-affected single-slip behavior of pure nickel microcrystals. Acta Mater. 53, 4065–4077.
Dimiduk, D.M., Woodward, C., LeSar, R., Uchic, M.D., 2006. Scale-free intermittent flow in crystal plasticity. Science 312, 1188–1190.
Dimiduk, D.M., Nadgorny, E.M., Woodward, C., Uchic, M.D., Shade, P.A., 2010. An experimental investigation of intermittent flow and strain burst scaling behavior in LiF crystals during microcompression testing. Philos. Mag. 90, 3621–3649.
El-Awady, J.A., Uchic, M.D., Shade, P.A., Kim, S.-L., Rao, S.I., Dimiduk, D.M., Woodward, C., 2013. Pre-straining effects on the power-law scaling of size-dependent strengthening in Ni single crystals. Scripta Mater. 68, 207–210.
Freund, L.B., Suresh, S., 2003. Thin Film Materials. Cambridge University Press, Cambridge., p. 133.
Greer, J.R., Nix, W.D., 2006. Nanoscale gold pillars strengthened through dislocation starvation. Phys. Rev. B. 73, 245410.
Huang, Y., 1991. A user-material subroutine incorporating single crystal plasticity in the ABAQUS finite element program. Mech. Report 178, Division of Applied Sciences, Harvard University, Cambridge, MA.
Hurtado, D.E., Ortiz, M., 2012. Surface effects and the size-dependent hardening and strengthening of nickel micropillars. J. Mech. Phys. Solids 60, 1432–1446.
Hutchinson, J.W., 1976. Bounds and self-consistent estimates for creep of polycrystalline materials. Proc. Roy. Soc. London A348, 1465–1469.
Jennings, A.T., Li, J., Greer, J.R., 2011. Emergence of strain-rate sensitivity in Cu nanopillars: transition from dislocation multiplication to dislocation nucleation. Acta Mater. 59, 5627–5637.
Jérusalem, A., Fernández, A., Kunz, A., Greer, J.R., 2012. Continuum modeling of dislocation starvation and subsequent nucleation in nano-pillar compressions. Scripta Mater. 66, 93–96.
Kuroda, M., 2013. Higher-order gradient effects in micropillar compression. Acta Mater. 61, 2283–2297.
Kysar, J.W., 1997. Addendum to 'A user-material subroutine incorporating single crystal plasticity in the ABAQUS finite element program'. Mech. report 178, Cambridge (MA), Division of Applied Sciences, Harvard University, 1997.
Ma, A., Roters, F., Raabe, D., 2006a. A dislocation density based constitutive model for crystal plasticity FEM including geometrically necessary dislocations. Acta Mater. 54, 2169–2179.
Ma, A., Roters, F., Raabe, D., 2006b. Studying the effect of grain boundaries in dislocation density based crystal-plasticity finite element simulations. Int. J. Solids Struct. 43, 7287–7303.
Ma, A., Roters, F., Raabe, D., 2006c. On the consideration of interactions between dislocations and grain boundaries in crystal plasticity finite element modeling-theory, experiments, and simulations. Acta Mater. 54, 2181–2194.
Ng, K.S., Ngan, A.H.W., 2008. Stochastic nature of plasticity of aluminum micropillars. Acta Mater. 56, 1712–1720.
Ngan, A.H.W., Ng, K.S., 2010. Transition from deterministic to stochastic deformation. Philos. Mag. 90, 1937–1954.
Norfleet, D.M., Dimiduk, D.M., Polasik, S.J., Uchic, M.D., Mills, M.J., 2008. Dislocation structures and their relationship to strength in deformed nickel microcrystals. Acta Mater. 56, 2988–3001.
Papanikolaou, S., Dimiduk, D., Choi, W., Sethna, J., Uchic, M., Woodward, C., Zapperi, S., 2012. Quasi-periodic events in crystal plasticity and the self-organized avalanche oscillator. Nature 490, 517–521.
Peirce, D., Asaro, R.J., Needleman, A., 1983. Material rate dependence and localized deformation in crystalline solids. Acta Metall. 31, 1951–1976.
Raabe, D., Ma, D., Roters, F., 2007. Effects of initial orientation, sample geometry and friction on anisotropy and crystallographic orientation changes in single crystal microcompression deformation: a crystal plasticity finite element study. Acta Mater. 55, 4567–4583.
Roters, F., Eisenlohr, P., Hantcherli, L., Tjahjanto, D., Bieler, T., Raabe, D., 2010. Overview of constitutive laws, kinematics, homogenization and multiscale methods in crystal plasticity finite-element modeling: theory, experiments, applications. Acta Mater. 58, 1152–1211.
Schwerdtfeger, J., Nadgorny, E., Koutsos, V., Blackford, J.R., Zaiser, M., 2010. Statistical heterogeneity of plastic deformation: an investigation based on surface profilometry. Acta Mater. 58, 4859–4870.
Shade, P.A., Wheeler, R., Choi, Y.S., Uchic, M.D., Dimiduk, D.M., Fraser, H.L., 2009. A combined experimental and simulation study to examine lateral constraint effects on microcompression of single-slip oriented single crystals. Acta Mater. 57, 4580–4587.
Shade, P.A., Uchic, M.D., Dimiduk, D.M., Viswanathan, G.B., Wheeler, R., Fraser, H.L., 2012. Size-affected single-slip behavior of René N5 microcrystals. Mater. Sci. Eng. A 535, 53–61.
Shan, Z.W., Mishra, R.K., Asif, S.A.S., Warren, O.L., Minor, A.M., 2008. Mechanical annealing and source-limited deformation in submicrometre-diameter Ni crystals. Nature Mater. 7, 115–119.
Tang, H., Schwarz, K.W., Espinosa, H.D., 2008. Dislocation-source shutdown and the plastic behavior of single-crystal micropillars. Phys. Rev. Lett. 100, 185503.
Uchic, M.D., Dimiduk, D.M., 2005. A methodology to investigate size scale effects in crystalline plasticity using uniaxial compression testing. Mater. Sci. Eng. A 400–401, 268–278.
Uchic, M.D., Dimiduk, D.M., Florando, J.N., Nix, W.D., 2004. Sample dimensions influence strength and crystal plasticity. Science 305, 986–989.
Wang, Z.-J., Li, Q.-J., Shan, Z.-W., Li, J., Sun, J., Ma, E., 2012. Sample size effects on the large strain bursts in submicron aluminum pillars. Appl. Phys. Lett. 100, 071906-071903.
Zaiser, M., Aifantis, E.C., 2006. Randomness and slip avalanches in gradient plasticity. Int. J. Plast. 22, 1432–1455.
Zhang, X., Aifantis, K.E., 2011. Interpreting strain bursts and size effects in micropillars using gradient plasticity. Mater. Sci. Eng. A 528, 5036–5043.
Zhang, X., Shang, F., 2013. Study on the temporal aspects of strain burst in Ni micropillar deformation. Unpublished work.
Zhang, X., Pan, B., Shang, F., 2012. Scale-free behavior of displacement bursts: lower limit and scaling exponent. EPL (Europhys. Lett.) 100, 16005.
Zhu, T., Li, J., Samanta, A., Leach, A., Gall, K., 2008. Temperature and strain-rate dependence of surface dislocation nucleation. Phys. Rev. Lett. 100, 025502.